Mind the gap : gas and dust in planet-forming disks

Marel, N.

4

Testing particle trapping in transition disks

Pinilla, P.; van der Marel, N.; Pérez, L.M.; van Dishoeck, E.F.; Andrews, S.M.; Birnstiel, T.; Herczeg, G.J.; Pontoppidan, K.M.; van Kempen, T. *Testing particle trapping in transition disks with ALMA.* A&A, in revision.

Abstract

Some protoplanetary disks show evidence of inner dust cavities. Recent observations of gas and dust of these so-called transition disks have given major support to the hypothesis that the origin of such cavities is trapping in pressure bumps. We present new Atacama Large Millimeter/submillimeter Array (ALMA) continuum observations at 336 GHz of two transition disks, SR21 and HD 135344B. In combination with previous ALMA observations from Cycle 0 at 689 GHz, we compare the visibility profiles at the two frequencies and calculate the spectral index ($\alpha_{\rm mm}$). The observations of SR 21 show a clear shift in the visibility nulls, indicating radial variations of the inner edge of the cavity at the two wavelengths. Notable radial variations of the spectral index are also detected for SR 21 with values of $\alpha_{\rm mm} \sim 3.8 - 4.2$ in the inner region ($r \lesssim 35$ AU) and $\alpha_{\rm mm} \sim 2.6 - 3.0$ outside. An axisymmetric ring (*"ring model"*) or a ring with the addition of an azimuthal Gaussian profile, for mimicking a vortex structure (*"vortex model"*), is assumed for fitting the disk morphology. For SR 21, the ring model better fits the emission at 336 GHz, conversely the vortex model better fits the 689 GHz emission. For HD 135344B, neither a significant shift in the null of the visibilities nor radial variations of $\alpha_{\rm mm}$ are detected. Furthermore, for HD 135344B, the vortex model fits both frequencies better than the ring model. However, the azimuthal extent of the vortex increases with wavelength, contrary to model predictions for particle trapping by anticyclonic vortices. For both disks, the azimuthal variations of $\alpha_{\rm mm}$ remain uncertain to confirm azimuthal trapping. The comparison of the current data with a generic model of dust evolution that includes planet-disk interaction suggests that particles in the outer disk of SR 21 have grown to millimetre sizes and have accumulated in a radial pressure bump, whereas with the current resolution there is not clear evidence of radial trapping in HD 135344B, although it cannot be excluded either.

4.1 Introduction

Recent observations of transition disks (disks with inner dust cavities) suggest that their structures may originate from particle trapping in pressure bumps (e.g. van der Marel et al. 2013; Zhang et al. 2014). Particle accumulation in pressure maxima has been suggested to solve the problem of rapid inward drift of particles (e.g. Weidenschilling 1977; Brauer et al. 2008), implying that planetary embryos may form in localised environments (e.g. Klahr & Henning 1997; Johansen et al. 2007). Pressure bumps may occur due to the presence of one or multiple planets in the disk (e.g. Dodson-Robinson & Salyk 2011; Pinilla et al. 2012a, 2015a; Zhu et al. 2012), but other phenomena such as dead zones may also create pressure traps and explain their structures (e.g. Regály et al. 2012; Flock et al. 2015). Observations of transition disks reveal that dust cavities appear to be smaller at shorter wavelengths (e.g. Dong et al. 2012; Garufi et al. 2013). This spatial segregation of small and mm-sized grains is a natural consequence of particle trapping in the planet-disk interaction scenario (e.g. Rice et al. 2006; de Juan Ovelar et al. 2013).

The spectral index $\alpha_{\rm mm}$ ($F_\nu \propto \nu^{\alpha_{\rm mm}}$) provides information on the particle size in protoplanetary disks (see Testi et al. 2014, for a review). For (sub-)micron sized dust, as found in the interstellar medium, $\alpha_{\rm mm}$ is expected to have values of $\gtrsim 3.5 - 4.0$ (e.g. Finkbeiner et al. 1999). When dust grows to millimetre sizes, $\alpha_{\rm mm}$ is expected to decrease (Draine 2006; Ricci et al. 2010b). Radial increases in $\alpha_{\rm mm}$ (on 100 AU scales) have been found for individual disks without cavities (e.g. Guilloteau et al. 2011; Pérez et al. 2012), consistent with radial drift. In contrast, the inner region of transition disks is depleted of large grains, so that $\alpha_{\rm mm}$ would decrease with radius from the central star (Pinilla et al. 2014). However, such radial variations for $\alpha_{\rm mm}$ in transition disk have not been spatially resolved to date.

In this paper, we combine observations from ALMA Cycle 0 at 689 GHz (~450 μm) and Cycle 1 at 336 GHz (~ 870μm) of SR 21 and HD 135344B (also known as SAO 206462) to compare the morphological structures at the two frequencies and calculate $\alpha_{\rm mm}$ throughout the disk. In addition, we compare the results with a generic model of particle trapping and dust growth in a pressure bump induced by an embedded planet, and place the results in the context of other transition disks.

4.2 Targets and observations

SR 21 is a G3 star located in the Ophiuchus star-forming region at a distance of $d = 120$ pc (Loinard et al. 2008). The disk was identified as a transition disk by its mid-infrared SED, with a cavity radius of $\sim$ 18 AU (Brown et al. 2007). Observations with the Submillimeter Array (SMA) at 850 μm confirmed a $\sim$ 35 AU cavity and suggested an azimuthal disk asymmetry (Brown et al. 2009; Andrews et al. 2011), which was much more clearly seen with ALMA observations in Cycle 0 (Pérez et al. 2014). While 450 μm imaging with ALMA shows strong depletion of large mm-sized grains, by a factor of 10^3 or more in the inner region (van der Marel et al. 2015c), H-band scattered light imaging indicates that the small grains are much less depleted, perhaps by as little as a factor of 10 (Follette et al. 2013).

HD 135344B is an F4 star located in the Sco OB2-3 star-forming region at a distance of $d = 140$ pc (van Boekel et al. 2005). A cavity radius of $\sim$ 45 AU was also identified by its SED (Brown et al. 2007) and confirmed by SMA observations (Brown et al. 2009). One of the most intriguing characteristics of this disk is its spiral arms observed in scattered light images (Muto et al. 2012; Garufi et al. 2013). The observations with VLT/NACO did not show signs of a gap in small dust grains down to 28 AU radius (Garufi et al. 2013).

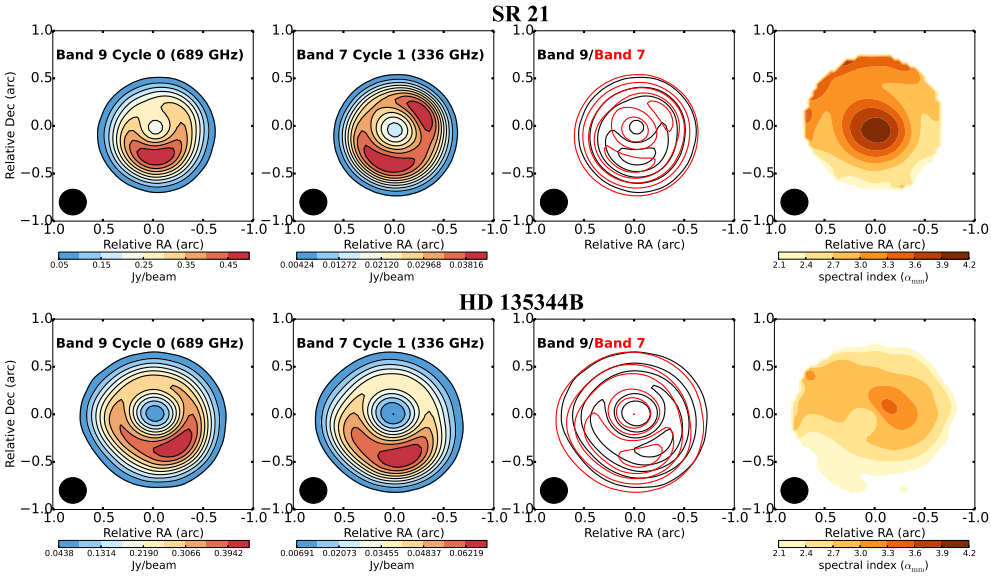

Figure 4.1: *ALMA observations of dust continuum emission for SR 21 (top panels) and HD 135344B (bottom panels). The left columns show the Band 9 (689 GHz) and Band 7 (336 GHz) continuum, with the contour overlaid at 10,20,...,90% of the peak. The third column shows the overlay of the contours with a step of 20% of the peak (black is Band 9, red is Band 7). The right column shows the resolved $\alpha_{\rm mm}$ in colour contours. The beam size is indicated in each plot.*

Table 4.1: *Observation properties*

Target	Band	ν (GHz)	$\Delta\nu$ (GHz)	$F_{\rm peak}$ (mJy)	$F_{\rm total}$ (mJy)	σ (mJy)	Date
SR 21	7	336	3.2	42.4	349	0.08	26/07/2014
	9	689	7.5	500	2877	2.0	18/07/2012
HD 135344B	7	336	3.2	69.1	636	0.13	27/07/2014
	9	689	7.5	438	3360	2.5	05/07/2012

The observations used in this letter are from ALMA Cycle 0 program 2011.0.00724.S (P.I. Pérez) and Cycle 1 program 2012.1.00158.S (P.I. van Dishoeck), taken in Band 9 and Band 7, respectively. The details of the calibration are described in Pérez et al. (2014) and van der Marel et al. (2015b). For both observation sets, the images were obtained using Briggs weighting with a robust parameter of 0.5 and and the beam is set to be the same at both Bands by the post-processing of the images, which is the best possible beam size corresponding to both the Band 7 and Band 9 observations (0.27"). The details of the images are given in Table 4.1.

As the data are taken almost two years apart, the centre of the 2014 data was shifted before overlaying the images to compensate for the proper motion of the stars. The proper motion is -12,-24 mas yr^{-1} for SR 21 (Makarov 2007) and -20,-24 mas yr^{-1} for HD 135344B (Høg et al. 2000). Figure 4.1 shows the continuum maps and their overlay. The shape and contrast of the asymmetry look similar between Band 7 and 9 for HD 135344B. In contrast, SR 21 looks more symmetric in Band 7. There is an azimuthal shift in the continuum overlay for both sources. The position of the gain calibrator (the same for both observations) shifts $\lesssim$0.1 mas, meaning that the azimuthal shift is not due to calibration. With respect to the SMA images in 2006/2007 (Brown et al. 2009), the asymmetries are also shifted.

4.3 Data analysis

4.3.1 Visibilities and disk morphology

The real part of the visibilities at both frequencies is shown in Figure 4.2. These are extracted from the continuum data and deprojected using $i = 15°$ and position angle P.A.=14° for SR 21, and $i = 20°$ and P.A.=63°, as derived in Pontoppidan et al. (2008) and van der Marel et al. (2015c). The data are binned by taking the mean of the available data points in bins of 20 kλ, with a minimum of 5 data points per bin. In Figure 4.2, we show the real part of the visibilities for the two bands. The length of the projected baseline where the visibilities cross zero (the null) indicates the location inner edge of the cavity in a given bandpass (smaller values for the null mean that the cavity inner edge is further out for the same disk properties). The nulls for SR 21 are ~220 kλ at Band 9 and ~250 kλ at Band 7. For HD 135344B the null is almost at the same position at both wavelengths (~190 kλ). The imaginary part of the visibilities are presented in Appendix 4.B.

To fit the visibility profiles and constrain the structure of both disks, we used the same morphological models described in Pérez et al. (2014). One model is a ring-like emission described by $F(r,\theta) = F_R\, e^{-(r-r_R)^2/2\sigma_R^2}$, being r_R the location of the peak of the ring emission, F_R the flux density at r_R, and σ_R the ring width *("ring model")*. The other model assumes a ring together with an azimuthal Gaussian profile to mimic a vortex structure (Lyra & Lin 2013). The vortex is described by $F(r,\theta) = F_V\, e^{-(r-r_V)^2/2\sigma_{r,V}^2} e^{-(\theta-\theta_V)^2/2\sigma_{\theta,V}^2}$, with r_V and θ_V being the radius and P.A. at the peak of the vortex, F_V the flux density at (r_V,θ_V), and $\sigma_{\theta,V}, \sigma_{r,V}$ is the width of the vortex in the radial and azimuthal direction respectively *("vortex model")*. The parameters of the best fit model are found by minimising χ^2 using the same Markov Chain Monte Carlo (MCMC) approach implemented by Pérez et al. (2014). The results are summarised in Table 4.2. The errors from the MCMC calculations are much smaller than the spatial uncertainty from the observations, which is typically $\sim$ 10% of the beam size (i.e. $\sim$3 AU for SR 21 and $\sim$4 for HD 135344B) for the high signal to noise of the data (Table 4.1). For the MCMC calculations, the inclination and P.A. are fixed to the values found by Pérez et al. (2014) for both disks. The model including a vortex did not converge to a physical

Table 4.2: *Best fit parameters the disk morphology models of ring or ring+vortex.*

(a) Ring model

Target	ν (GHz)	χ^2	F_R (μm)	r_R (AU)	σ_R (AU)
SR 21	336	2.07	0.71	41	12
	689	1.39	5.91	36	15
HD 135344B	336	3.75	0.84	61	19
	689	1.18	5.72	60	18

(b) Ring+Vortex model

Target	ν (GHz)	χ^2	F_R (μm)	r_R (AU)	σ_R (AU)	F_V (μm)	r_V (AU)	θ_V ($^\circ$)	$\sigma_{R,V}$ (AU)	$\sigma_{\theta,V}$ (AU)
SR 21	689	1.06	4.72	35	14	4.0	46	178	14	40
HD 135344B	336	1.52	0.70	70	14	0.88	43	172	16	53
	689	1.05	5.24	65	16	7.0	42	194	7.0	47

Notes. All data of Band 9 are identical than Pérez et al. (2014). The parameters for SR 21 in Band 7 of the ring+vortex model are omitted because of the unphysical results. The errors from the MCMC calculations are much smaller than the spatial uncertainty from the observations (and therefore omitted), which is ~ 10% of the beam size (i.e. ~3 AU for SR 21 and ~4 AU for HD 135344B).

solution for SR 21 in Band 7, because the azimuthal extension of the vortex covers more than 2π. In summary, the SR 21 data are best fit with a ring model, while the HD 135344B data are best fit with a vortex model (see Figure 4.2). The residuals obtained by subtracting the best fit model from the data in Band 7 are shown for both targets in Appendix 4.C.

In the case of SR 21, the best-fit model indicates that larger grains, as traced at longer wavelengths by Band 7, are more spatially confined than the smaller grains traced at shorter wavelengths by Band 9 ($\sigma_R \sim 12$ AU at 870 μm vs. $\sigma_R \sim 15$ AU at 450 μm). Furthermore, the peak of emission in the ring is at larger radii in Band 7 than in Band 9 ($r_R \sim 41$ AU at 870 μm vs. $r_R \sim 36$ AU at 450 μm). The location of the inner edge of the cavity at the two frequencies varies from ~ 29 AU in Band 9 to ~ 35 AU in Band 7, which together with the wider ring, is consistent with the shift of the null of the visibilities (Figure 4.2). For HD 135344B, the vortex model is consistently the best-fit model for both wavelengths. The inner edge of the cavity is almost constant in the two bands, as shown in the visibility nulls (Figure 4.2). However, the width of the vortex in both the radial and azimuthal directions is significantly larger in Band 7, and its aspect ratio ($\sigma_{\theta,V}/\sigma_{r,V}$) decreases from 7.1 in Band 9 to 3.3 in Band 7.

4.3.2 Spectral index

The position-dependent spectral index (right panels of Figure 4.1) is calculated using both bands as $\alpha_{\rm mm} = \ln \frac{F_{\nu_{B7}}}{F_{\nu_{B9}}} / \ln \frac{\nu_{B7}}{\nu_{B9}}$. All data with $F < 5\sigma$ are excluded. The dust emission within the cavity is detected at a high level of significance (S/N~ 320σ and ~ 250σ in Band 7, and ~ 120σ and ~ 80σ in Band 9, for SR 21 and HD 135344B, respectively), so $\alpha_{\rm mm}$ can be accurately computed in the cavity separately from the dust ring. The uncertainty of $\alpha_{\rm mm}$ is calculated by error propagation from the observational uncertainty, which includes the calibration uncertainties (~20% and ~10% in Band 9 and 7 respectively) and the noise level or rms (σ) of the observations. With the high signal-to-noise of the data, the uncertainty on the spectral index $\sigma_{\alpha_{\rm mm}}$ at a given position is dominated by the calibration uncertainties

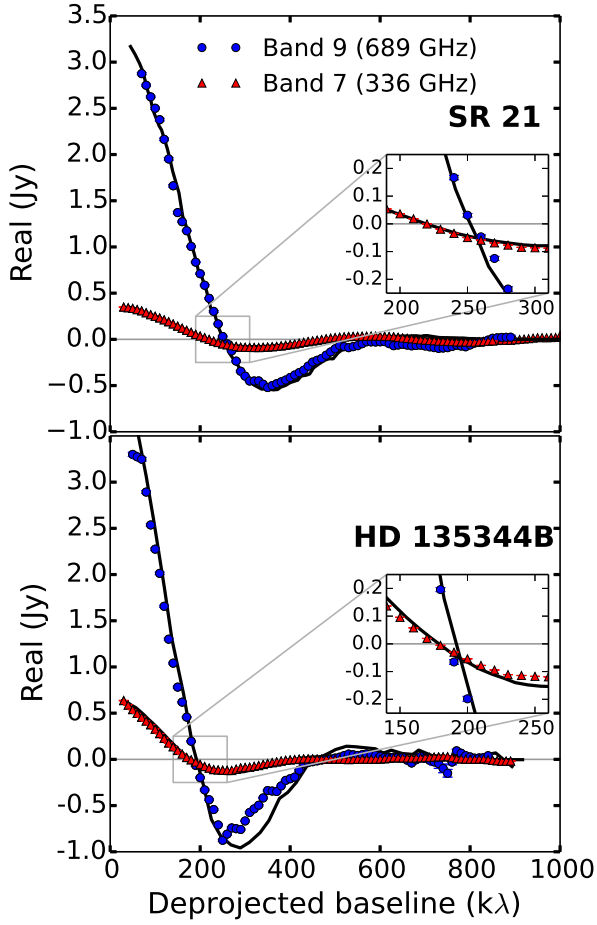

Figure 4.2: *Real part of the visibilities at 689 GHz (~450 μm, Band 9) and at 336 Gz (~870 μm, Band 7) for SR 21 (top panel) and HD 135344B (bottom panel). Note that the plot includes error bars which are of the size of the plotting points. At both wavelengths, the models with the best fit parameters are over-plotted (solid line), which is the ring model in the case of SR 21, and the vortex model for HD 135344B.*

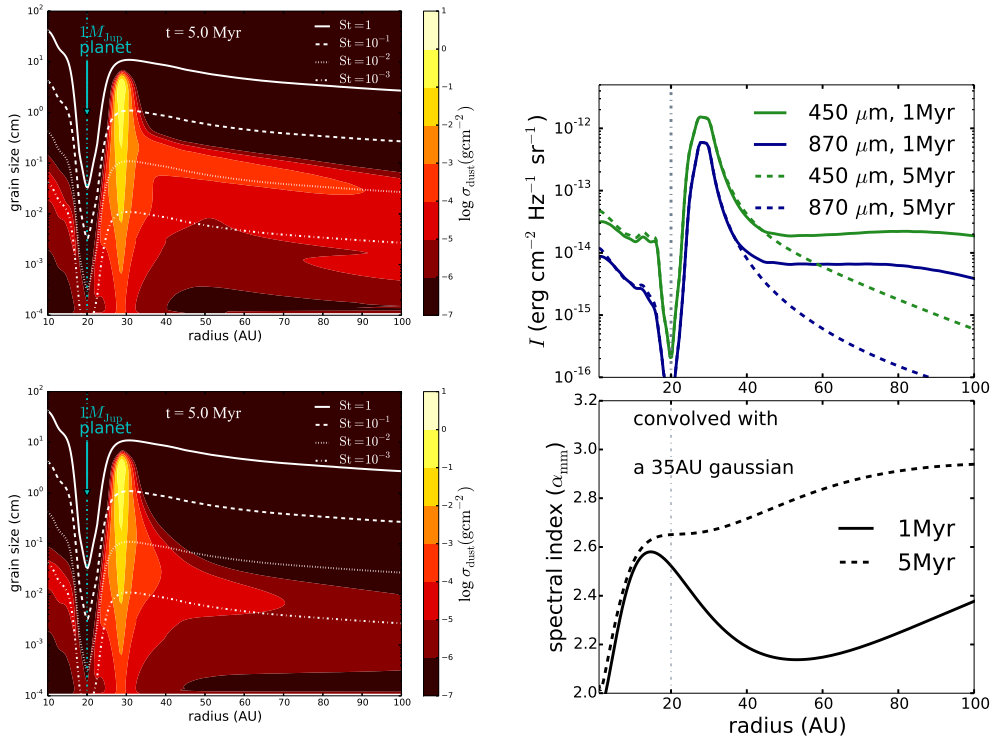

Figure 4.3: Left. *Dust density distribution when* 1 $M_{\rm Jup}$ *is embedded at 20 AU after 1 and 5 Myr of evolution (top and bottom panel respectively). The lines represent particle sizes with different Stokes numbers (St=*$[10^{-3}, 10^{-2}, 10^{-1}, 1]$*), which are proportional to the gas surface density profile.* **Right.** *Top panel: Intensity radial profiles at 450 and 870* μ*m, obtained from the dust density distributions after 1 and 5 Myr of evolution. Bottom panel: radial profile of* $\alpha_{\rm mm}$ *calculated from the intensity profiles at 450 and 870* μ*m, which is convolved a with 35 AU Gaussian beam.*

and approximates to $\approx (\ln \nu_1/\nu_2)^{-1}\sqrt{(0.2^2+0.1^2)} \approx 0.3$, in both cases. However, for the relative spatial changes in $\alpha_{\rm mm}$, the systematic calibration uncertainty does not contribute since it is constant across the field, and changes in $\alpha_{\rm mm}$ inside and outside the dust cavity have high significance with maximum values of $\sigma_{\alpha_{\rm mm}}$ of $\approx$ 0.01. SR 21 shows significant radial variations of $\alpha_{\rm mm}$, with values of $\alpha_{\rm mm} \sim 3.8-4.2$ within ~0.3" radius (~35 AU) and $\alpha_{\rm mm} \sim 2.6-3.0$ outside ($\Delta\alpha_{\rm mm} \gtrsim 120\sigma_{\alpha_{\rm mm}}$). This implies a lack of mm-grains in the inner region ($r \lesssim 35$ AU), and is consistent with accumulation of mm grains in a localised region in the outer disk. For HD 135344B, no significant radial variations for $\alpha_{\rm mm}$ are found, and the values remain within a range of 2.6 – 3.2. Although Figure 4.1 shows azimuthal variations of $\alpha_{\rm mm}$ for both sources, these depend considerably on how the two images are overlaid in the calculation of $\alpha_{\rm mm}$ (see Appendix 4.A), and therefore any azimuthal variation within a range of $\alpha_{\rm mm} \simeq 2.6-3.2$ remains uncertain.

4.4 Theoretical predictions of particle trapping

Dust trapping, in radial and azimuthal pressure bumps, depends on the coupling of the particles to the gas, the pressure gradient, and the disk turbulence. The dimensionless stopping time, Stokes number, quantifies the coupling of the particles and it is defined as $\mathrm{St} = a\rho_s\pi/2\Sigma_g$ (with ρ_s being the volume density of a grain, with typical values of $\sim$ 1g cm^{-3}, Blum & Wurm 2008, and Σ_g the gas surface density). Particles with St $\sim$ 1 preferentially move to the regions of pressure maxima (e.g. Birnstiel et al. 2010; Pinilla et al. 2012a). However, because the gas is turbulent, it is expected that the dust is turbulently mixed by the gas. The dust diffusion prevents the concentration of all the particles with St $\sim$ 1 inside pressure traps. The drift of particles (and hence the trapping) is efficient for particles with St $\gtrsim$ ff$_{\mathrm{visc}}$, where α_{visc} is a dimensionless number that quantifies the disk viscosity (Shakura & Sunyaev 1973). From the combination of radial drift and dust diffusion, it is expected that particles with St $\sim$ 1 are more concentrated at the pressure maximum than St $<$ 1. For example, the models of dust trapping by a vortex predict that larger grains would be more azimuthally concentrated in the centre of the vortex (Birnstiel et al. 2013; Lyra & Lin 2013), as observed in IRS 48 (van der Marel et al. 2015a) and HD 142527 (Casassus et al. 2015).

The left panels of Figure 4.3 show the model predictions for particle trapping triggered by planet-disk interaction. The gas surface density is obtained from hydrodynamical simulations of a 1 M_{Jup} planet embedded in the disk at 20 AU distance from the star as in Pinilla et al. (2012a). The initial gas surface density and temperature are assumed to be a power law, and the disk viscosity is taken to be $\alpha_{\mathrm{visc}} = 10^{-3}$. The dust density distributions are obtained from dust evolution models that include the dynamics and coagulation of dust particles Birnstiel et al. (2010). When a planet opens a gap in the disk, a pressure bump is formed at the outer edge of the gap, and large particles drift to the pressure maximum located in this case at $\sim$ 30 AU. The particle sizes with different Stokes number (St=$[10^{-3}, 10^{-2}, 10^{-1}, 1]$) are shown to illustrate how the radial concentration becomes narrower for particles with higher St. The right panels of Figure 4.3 show the intensity profile at 450 and 870 μm. The emission profile is only slightly narrower at 870 μm since the range of particles sizes that are traced is comparable. Both the dust density distributions and the intensity profiles become narrower at longer times of evolution.

Due to particle trapping, the region close to the planet is empty of mm/cm particles, and therefore α_{mm} is expected to increase close to the location of the gap carved by the planet. Figure. 4.3 also shows the expected radial profiles of α_{mm} calculated from the models at 450 and 870 μm and convolved with a 2D Gaussian profile of 35 AU diameter. In the inner part ($r \lesssim 10$ AU), α_{mm} drops because of the presence of the mm-particles. Because there is no total filtration of particles at the outer edge of the gap, small-grains still flow through the gap and grow again to mm-sizes in the inner region ($r \lesssim 10$ AU). One way to prevent the presence of mm-grains is to increase the mass of the planet, to completely filter all particle sizes (Zhu et al. 2012; Pinilla et al. 2012a, 2015a).

At early times of dust evolution ($\sim$ 1 Myr), mm/cm-grains are still distributed in the entire outer disk ($r \gtrsim 30$ AU) and radial variations of α_{mm} are detected after convolution. This is not the case at 5 Myr, since the concentration of mm/cm particles becomes much narrower compared to the spatial resolution and hence the potential radial variation of α_{mm} is smeared out and is not detected.

4.5 Discussion

With the new ALMA observations of SR 21 and HD 135344B, it is possible to test if radial/azimuthal trapping is the cause of the disk structures (cavities and asymmetries). Observationally, radial trapping can be tested by analysing the location of the null in the real part of the visibilities at different wavelengths, because in the case of trapping, the mm-emission is expected to show a wider ring at shorter wavelengths. Thus, the inner edge of the ring (or dust cavity) should be located closer to the star at shorter wavelengths (Section 4.4). Additional insights can be gained by analysing the wavelength-dependent morphology and the position-dependent spectral index.

SR 21: The current observations of SR 21 at 336 and 689 GHz suggest that the disk morphology at longer wavelengths is better described by a ring than by a vortex. From observations of ^{12}CO, the disk mass of SR 21 has been inferred to be $\sim$ 12 $M_{\rm Jup}$, and the average value of the gas surface density close to the cavity is $\sim$ 80 g cm^{-2} (van der Marel et al. 2015c). Analysis of recent observations of ^{13}CO and C^{18}O of this disk confirmed the disk mass (van der Marel et al. 2015b). Assuming that at each wavelength, particles with a maximum size of $\lesssim 3\lambda$ are traced (e.g. Draine 2006), the observations at Band 7 and 9 traced particles with St $\sim 2.5\times10^{-3} - 5.0\times10^{-3}$ close to the location of the cavity. These particles are expected to be still affected by radial drift and to move toward pressure maxima.

The fact that at a longer wavelength the morphology is better described by a ring than a vortex is in contradiction with model predictions of trapping by a vortex. Thus, the observed azimuthal structure is likely not caused by a vortex. Moreover, to sustain a long-lived vortex, the radial width of the vortex cannot be much higher than the disk scale-height ($\lesssim 2h$, Barranco & Marcus 2005) and the fact that the radial width of the vortex in SR 21 is much larger than the disk scale height ($\sim \times 5\ h$, van der Marel et al. 2015c), as found from the morphology fitting of the Band 9 data (Table 4.2), also disfavours the vortex scenario.

In the radial direction, larger grains traced at 870 μm are more narrowly concentrated than smaller grains traced at 450 μm in SR 21, as demonstrated in the shift of the nulls of the visibilities (see Figure 4.2 and Table 4.2). The narrower concentration of larger grains is in agreement with particle trapping by a radial pressure bump. Further evidence that radial trapping occurs in SR 21 is given by the radial changes of the spectral index $\alpha_{\rm mm}$, which increase outwards, as expected from radial trapping models (Figure 4.3b). The detection of radial variation of $\alpha_{\rm mm}$ with the current resolution suggests that particle trapping in SR 21 have occurred in $\lesssim$ 1 Myr, because at longer times, variations of $\alpha_{\rm mm}$ would not be detected (Figure 4.3b). The discrepancy between the model predictions and the observations for the values of $\alpha_{\rm mm}$ in the inner part of the disk come from the fact that we do not have total filtration of particles in the outer edge of the gap in our model.

Another potential explanation for variations of $\alpha_{\rm mm}$ is high optical depth, in which case the physical temperature is expected to be close to the brightness temperature. To reproduce the observed differences in $\alpha_{\rm mm}$ only by optical depth effects the emission must originate from a small surface area. Assuming that the emission is distributed in a homogeneous ring whose temperature is equal to the highest brightness temperature at the peak of emission obtained at the two frequencies ($T_B \approx$32 K in Band 9 and $\approx$13 K in Band 7), the ring must be very narrow ($\lesssim$3 AU in width), which contradicts the observed spatial extent of the emission in both bands (30-40AU for SR 21 and 60-70AU for HD 135344B, see Table 4.2). Thus, the radial variations of $\alpha_{\rm mm}$ cannot be due to optically thick emission alone. Pérez et al. (2014) demonstrated that the emission at Band 9 is marginally optically thick at the peak of emission, so it can only trace some of the mass surface density, and hence high angular resolution observations at

longer wavelength are necessary to confirm our predictions at the location of the peak.

HD 135344B: In this case, the model with the best fit parameters for the disk morphology at the two wavelength is the vortex model (Table 4.2). The disk mass inferred from ^{12}CO, ^{13}CO, and C^{18}O is $\sim 20\ M_{\rm Jup}$ (van der Marel et al. 2015c,b), and the average value of the gas surface density at the location of the dust cavity is similar to that in SR 21 (~ 80 g cm^{-2}). Therefore, the current observations trace particles with similar Stokes numbers as SR 21.

From the morphological models, the azimuthal width of the vortex increases at longer wavelengths in contradiction with predictions of particle trapping by vortices. Similar as in SR 21 the radial width of the vortex is too large compared to the scale-height of the disk. The origin of the azimuthal asymmetry is inconsistent with a vortex and may be related to the spiral arms observed at scattered light as also suggested by Pérez et al. (2014). In particular the bright spiral in the south coincides with the location of the asymmetry in the millimetre (Garufi et al. 2013; Quanz 2015, see also Appendix 4.C). Indeed, the azimuthal shift of the peak (Figure 4.1, also observed for SR 21) may be related with physical rotation of spiral arms, but higher angular resolution observations are needed to confirm this prediction.

In contrast with SR 21, neither a shift of the null of the visibilities nor radial variations of $\alpha_{\rm mm}$ are detected for HD 135344B, but this does not exclude radial particle trapping. From the model predictions (Section 4.4), the dust density distribution of mm-grains is narrower concentrated at the pressure maximum after 5 Myr than at 1 Myr, and radial variatons in $\alpha_{\rm mm}$ would not be detected with the current resolution (Figure 4.3b). Hence, the fact that radial changes in $\alpha_{\rm mm}$ are not detected for HD 135344B can be related with the fact that any instability (e.g., planet) responsible for the trapping formed earlier (~5 Myr ago) in HD 135344B than in SR 21 (~1 Myr ago). Another possibility is that trapping happens in more refined structures such as spiral arms in gravitationally unstable disks, in which case any variations of $\alpha_{\rm mm}$ remains unresolved (Dipierro et al. 2015).

Besides longer evolution times, other disk and planet parameters, such as planet mass, turbulence, or disk temperature, can also affect the gap shape and thus the radial concentration of mm/cm-sized particles in pressure bumps, leading to a different spatial distribution of small and large grains. High contrast asymmetries have been observed in other transition disks and interpreted as vortices (e.g. Oph IRS 48, van der Marel et al. 2013). Detection of vortices in transition disks may be atypical because several parameters can prevent a vortex from being long-lived, such as strong turbulence or feedback from dust to the gas (e.g. Ataiee et al. 2013; Zhu & Stone 2014; Raettig et al. 2015). Even in the case where a planet originally triggered the formation of the vortex, an eccentric orbit or the presence of addition planets can also lead to its rapid destruction (Ataiee & Pinilla 2015). The current ALMA observations of SR 21 and HD 135344B suggest that anti-cyclonic vortices are not the origin of their low contrast azimuthal asymmetries. Observations at high angular resolution at longer, optically thin, wavelengths, which provide information about the distribution of larger grains, will further constrain the origin of the observed dust structures in transition disks.

4.A Uncertainties of azimuthal variations of spectral index

The calculation of the spectral index ($\alpha_{\rm mm}$) from the observations depends considerably on how the two images are overlapped. To demonstrate that the apparent azimuthal variations remain uncertain, we shifted the alignment of the Band 7 and Band 9 images of SR21 and

HD135344B by the positional uncertainty. Figure 4.4 shows $\alpha_{\rm mm}$ by shifting 20 mas in both vertical and horizontal direction. The only reliable variation of $\alpha_{\rm mm}$ is in the radial direction for SR 21, which remains significant independent of the alignment. In HD 135344B, there is a hint of high values of $\alpha_{\rm mm}$ opposite to the azimuthal asymmetry, that also remains independent of the alignment.

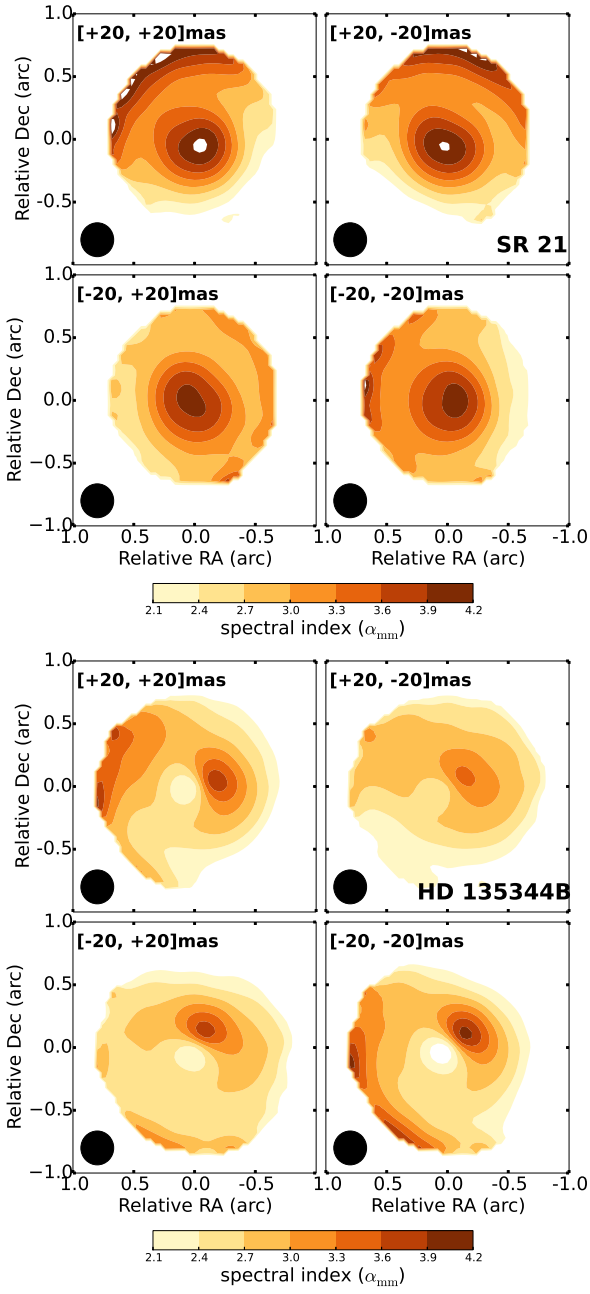

Figure 4.4: *Calculated spectral index ($\alpha_{\rm mm}$) assuming different alignments of the images for SR 21 (upper panel) and HD 135344B (lower panel).*

4.B Imaginary part of the visibilities

Figure 4.5 shows the imaginary part of the visibilities at 689 GHz (~450 μm, Band 9) and at 336 Gz (~870 μm, Band7) for SR 21 and HD 135344B. Non-zero imaginary visibilities indicate the presence of an azimuthal asymmetry (e.g. Isella et al. 2013). For HD 135344B, there are significant variations from zero at both frequencies. For SR 21, the non-zero values are marginal in Band 7, but significant in Band 9 data.

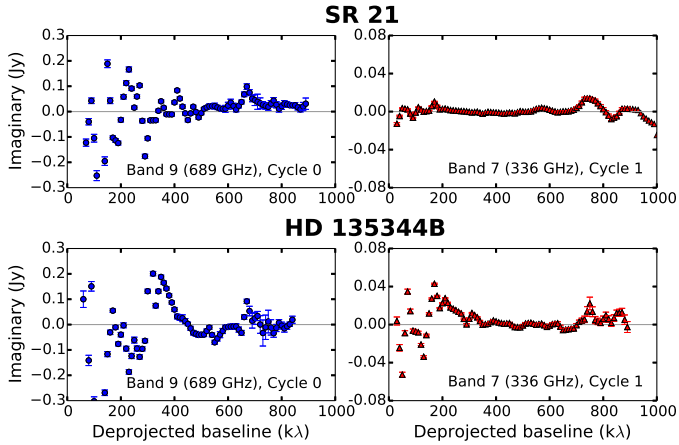

Figure 4.5: *Imaginary part of the visibilities at 689 GHz (~450 μm, Band 9) and at 336 GHz (~870 μm, Band7) for SR 21 (upper panel) and HD 135344B (lower panel).*

4.C Residual maps

Figure 4.6 illustrates the residual maps for both sources after subtracting the best fit models (Table 4.2) to the Band 7 data (336 GHz). For SR 21 the best fit is described by a ring model, whereas for HD 135344B it is a vortex model. The residuals for HD 135344B show a spiral structure as also suggested by Pérez et al. (2014) in Band 9 (689 GHz).

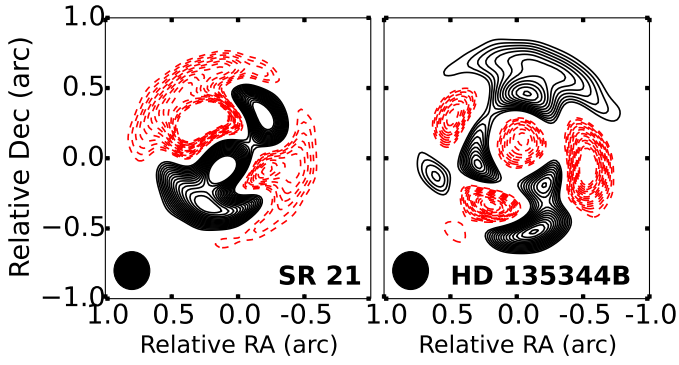

Figure 4.6: *Residual maps after subtracting the best fit models from Table 4.2, contours start at ±3σ and space by 3σ steps.*

Acknowledgements. We are thankful to the anonymous referee who helped to improve the quality of this manuscript. We are grateful to M. Benisty and C. P. Dullemond for fruitful discussions. Astrochemistry in Leiden is supported by the Netherlands Research School for Astronomy (NOVA), by a Royal Netherlands Academy of Arts and Sciences (KNAW) professor prize, and by the European Union A-ERC grant 291141 CHEMPLAN. T. B. acknowledges support from NASA Origins of Solar Systems grant NNX12AJ04G. This paper makes use of the following ALMA data: ADS/JAO.ALMA#2012.1.00158.S and #2011.0.00724.S. ALMA is a partnership of ESO (representing its member states), NSF (USA) and NINS (Japan), together with NRC (Canada) and NSC and ASIAA (Taiwan), in cooperation with the Republic of Chile. The Joint ALMA Observatory is operated by ESO, AUI/NRAO and NAOJ.